Monthly Notices
of the
ROYAL ASTRONOMICAL SOCIETY

MNRAS **428,** 3151–3163 (2013) doi:10.1093/mnras/sts266

Effects of entropy generation in jet-launching discs

P. Tzeferacos,[1,2]★ A. Ferrari,[1,2] A. Mignone,[1] C. Zanni,[3] G. Bodo[3] and S. Massaglia[1]

[1]*Dipartimento di Fisica, Università degli Studi di Torino, Via Giuria 1, I-10125 Torino, Italy*
[2]*Department of Astronomy and Astrophysics, University of Chicago, 5640 S. Ellis Ave, Chicago, 60637 IL, USA*
[3]*INAF – Osservatorio Astronomico di Torino, Viale Osservatorio 20, I-10025 Pino Torinese, Italy*

Accepted 2012 October 21. Received 2012 October 14; in original form 2012 July 29

ABSTRACT

A common approach to interpret the 'jet phenomenon' observed in active galactic nuclei and young stellar objects is via magnetohydrodynamic models of collimated outflows magnetically driven from quasi-Keplerian accretion discs in the proximity of a central gravitational attractor. In this study we present a series of time-dependent axisymmetric numerical simulations of a jet-launching accretion disc, where the outflow and the disc itself are treated consistently. In particular, the issue of thermal effects due to anomalous transport coefficients is being addressed. When the radiative losses of the accretion disc cannot perfectly balance Ohmic and viscous heating, the latter can severely influence the mass loading process. Since the ejection rates determine to a great extent the dynamics of the outflowing plasma, disc thermodynamics should not be neglected. We investigate numerically the impact of heating–cooling effects in both outflow dynamics and accretion disc structure. A relationship is established between heating and various important parameters of the outflow (magnetic lever arm, ejection efficiency, mass flux, etc.) that is briefly discussed in connection with observational data.

Key words: accretion, accretion discs – MHD – methods: numerical – ISM: jets and outflows.

1 INTRODUCTION

Plasma ejection from the surface of rotating stars via magnetohydrodynamic (MHD) mechanisms was originally investigated in the pioneering works of Mestel (1961) and Weber & Davis (1967) on magnetic stars and stellar winds. A decade later, Lovelace (1976) and Blandford (1976) showed independently, in the context of the dynamics of active galactic nuclei (AGN), that a force-free poloidal field, emerging from a Keplerian disc around a star or a black hole, can feed energy and angular momentum into a Poynting flux jet. Then, in a seminal work, Blandford & Payne (1982) calculated how a poloidal magnetic field, anchored on to a differentially rotating accretion disc around the core object, can give rise to a toroidal component, producing super-Alfvénic plasma winds through the *magnetocentrifugal mechanism*.

In this general scenario, several semi-analytical MHD studies have attempted to model the properties of jets and their launch, adopting different simplifications to derive exact solutions in limiting cases (axial symmetry, stationarity, self similarity, fixed boundary conditions in lieu of disc). Since the basis of self-similarity is the scaling of one variable with respect to one of the spatial coordinates, there are two distinct families of models: (i) self-similar in the radial direction (RSS), describing winds from accretion discs as in Blandford & Payne (1982) (see also Lovelace, Berk & Contopoulos 1991; Contopoulos & Lovelace 1994; Li 1995) and (ii) self-similar in the meridional direction (MSS), describing stellar outflows (Tsinganos & Trussoni 1990 in a series of studies). Vlahakis & Tsinganos (1998) reconstructed the classes of MSS and RSS of MHD outflows in a systematic way. Recently, Matsakos et al. (2008, 2009) successfully merged the two approaches numerically to simulate the stellar-jet/disc-wind interplay. The actual treatment of the accretion disc region came with the studies of Ferreira & Pelletier (1995), Ferreira (1997) and Casse & Ferreira (2000a), who found steady-state outflow solutions *linked* to accreting slim discs.

A different paradigm in jet-launching mechanisms places the origin of the outflow at the innermost radii of the accretion disc, where the accreted matter interplays with the star's magnetosphere. In the case of X-winds (Shu et al. 1994 in a series of studies, see also Shang et al. 2002 and references therein), the outflow is magnetocentrifugally accelerated from a small region beyond the co-rotation point where the angular velocity of the star matches that of the accretion disc. From similar launching radii, Romanova et al. (2009) modelled two-component outflows which consist of a fast axial jet that propagates along the stelar magnetic field lines and magnetically driven (as in Lovelace et al. 1991) conical winds from the X-region, both for slowly and rapidly rotating stars (*propeller* regime). More recently, this study was extended to investigate the ejection and collimation properties of the outflows for stars with large accretion rates (Königl, Romanova & Lovelace 2011; Lii, Romanova & Lovelace 2012) as in FU Orionis systems.

★ E-mail: petros.tzeferacos@ph.unito.it

© 2012 The Authors
Published by Oxford University Press on behalf of the Royal Astronomical Society

Downloaded from http://mnras.oxfordjournals.org/ at Uni Torino Dip Sanità Pubblica Microbiologia on February 19, 2013

The first attempt to tackle the magnetized disc–jet configuration in a non-linear time-dependent numerical model was made by Shibata & Uchida (1985) and Uchida & Shibata (1985), simulating the relaxation of a magnetic twist. Along the same lines, simulations were carried out by Stone & Norman (1994) and Kato, Kudoh & Shibata (2002), referring to the whole disc–jet system but for very short time-scales, starting from non-equilibrium conditions. Another approach has been to treat the accretion disc as a boundary condition and let the system converge to a stationary solution. Romanova et al. (1997) and Ouyed & Pudritz (1997) independently reported stationary solutions obtained from time-dependent simulations. The latter also treated the effects of mass loading (Ouyed & Pudritz 1999) and performed a three-dimensional stability analysis (Ouyed, Clarke & Pudritz 1997). A self-consistent numerical description of the disc–jet system came with the pioneering work of Casse & Keppens (2002). Those simulations made it clear that stationary (or quasi-stationary) solutions could be obtained consistently using some realistic initial conditions for the disc and its atmosphere.

In many of the above-mentioned studies, the disc thermodynamics and, to a great extent, the disc itself have been neglected. The few semi-analytical works, in which thermal effects were taken into account, managed to successfully cross the fast magnetosonic critical point (Vlahakis et al. 2000; Ferreira & Casse 2004), as well as to reproduce jet velocities in young stellar objects (YSO; Casse & Ferreira 2000b; Ferreira, Dougados & Cabrit 2006). Numerical disc–jet models, on the other hand, have been including the energy equation in their calculations but they customarily balance disc heating (Γ) with a specified cooling function (Λ) that emulates cooling processes, such as radiative losses or turbulent energy transport. With an entropy surplus of $Q = \Gamma - \Lambda \simeq 0$, the outflows produced are characterized as 'cold', exhibiting large magnetic lever arms and high terminal velocities, compatible with the solutions found by Ferreira (1997) (albeit moderated by numerical diffusion effects; Zanni et al. 2007; Tzeferacos et al. 2009; Murphy, Ferreira & Zanni 2010). Only Casse & Keppens (2004) and Meliani, Casse & Sauty (2006) have studied cases with $\Lambda = 0$, although the influence of disc heating Γ was limited due to small values of diffusivity.

In this study we examine, from a numerical point of view, how thermal effects in the disc region affect the jet launch and the outflow dynamics. By varying the amount of energy dissipated inside the disc, due to viscous and Ohmic heating, we can (i) mimic radiative inefficient discs as in the advection-dominated accretion flow (ADAF) scenario proposed by Narayan & Yi (1995). Such optically thin and geometrically thick regimes have been suggested also for YSO (Combet & Ferreira 2008), microquasars (Mirabel et al. 1998; Petrucci et al. 2010) and AGN (Di Matteo et al. 2000, 2003). Moreover, we can (ii) obtain superficial heating due to local turbulent dissipation or external illumination as in Casse & Ferreira (2000b), Casse & Keppens (2004) or Ferreira et al. (2006). This allows us to overcome the usual caveat of an adiabatic expansion and study 'warm' outflow solutions, which are necessary to explain T Tauri jet speeds (Garcia et al. 2001; Pesenti et al. 2004) and are also a possible source of the external Compton component, postulated by Donnarumma et al. (2009) and Vercellone et al. (2011) for blazars.

The plan of the paper is the following. In Section 2 we define the setup of the numerical code for our simulations and the basic physical parameters. Section 3 describes the 'warm' outflow solutions and Section 4 the back-reaction on discs. Section 5 discusses the results in connection with possible astrophysical applications.

2 SETUP

To follow the temporal evolution of our disc–jet model we solve numerically the equations of resistive and viscous MHD, under the single-fluid approximation on a cylindrical coordinate system. The form adopted in our numerical calculations is

$$\frac{\partial \rho}{\partial t} + \nabla \cdot (\rho \boldsymbol{u}) = 0, \tag{1}$$

$$\frac{\partial (\rho \boldsymbol{u})}{\partial t} + \nabla \cdot \left[\rho \boldsymbol{u}\boldsymbol{u} + \left(P + \frac{\boldsymbol{B}\cdot\boldsymbol{B}}{2} \right) \boldsymbol{I} - \boldsymbol{B}\boldsymbol{B} - \Pi \right] + \rho \nabla \Phi_g = 0, \tag{2}$$

$$\frac{\partial \boldsymbol{B}}{\partial t} + \nabla \times \boldsymbol{E} = 0, \tag{3}$$

$$\frac{\partial e}{\partial t} + \nabla \cdot \left[\left(e + P + \frac{\boldsymbol{B}\cdot\boldsymbol{B}}{2} \right) \boldsymbol{u} - (\boldsymbol{u}\cdot\boldsymbol{B})\boldsymbol{B} + (\eta_m \boldsymbol{J}) \times \boldsymbol{B} \right] - \nabla \cdot (\boldsymbol{u} \cdot \Pi) = -\Lambda_{\rm cool}. \tag{4}$$

The usual notation has been used for primitive variables, i.e. ρ the mass density, $\boldsymbol{u}$ the bulk speed of the flow, $\boldsymbol{B}$ the magnetic field vector and P the scalar thermal pressure. For a more compact notation, we can write the primitive variable vector as

$$\boldsymbol{V} = (\rho,\ u_r,\ u_\phi,\ u_z,\ B_r,\ B_\phi,\ B_z,\ P)\,. \tag{5}$$

In the momentum equation (equation 2) the forces taken into account are the thermal pressure gradient, the Lorentz force, viscous stresses and the gravitational force. The latter is described by its potential, created by the central object of mass M, which in cylindrical coordinates reads $\Phi_g = -GM/\sqrt{r^2 + z^2}$. The viscous transport coefficient η_u is included in Π, the viscous stress tensor. Its components, in the compressible limit, can be expressed in a general fashion as

$$\Pi_{ij} = 2\frac{\eta_u}{h_i h_j}\left(\frac{u_{i;j} + u_{j;i}}{2} \right) + \left(\eta_b - \frac{2}{3}\eta_u \right) \nabla \cdot \boldsymbol{u}\, \delta_{ij}. \tag{6}$$

Here η_u and η_b are the first and second viscosity parameters, although the latter is assumed to be equal to zero. On the other hand, h_i and h_j are the geometrical elements in the respective directions. $u_{i;j}$ and $u_{j;i}$ are the covariant derivatives of velocity.

The evolution of the magnetic field is governed by the induction equation (equation 3). The electric field is given by Ohm's law $\boldsymbol{E} = -\boldsymbol{u} \times \boldsymbol{B} + \eta_m \boldsymbol{J}$ and the current by $\boldsymbol{J} = \nabla \times \boldsymbol{B}$, where we introduced the magnetic resistivity tensor η_m.

In the energy equation (equation 4), the variable e stands for the total energy density, which is given by

$$e = \frac{P}{\gamma - 1} + \frac{\rho \boldsymbol{u}\cdot\boldsymbol{u}}{2} + \frac{\boldsymbol{B}\cdot\boldsymbol{B}}{2} + \rho\Phi_g, \tag{7}$$

the summation of internal, kinetic, magnetic and gravitational energy components. The system is completed by an ideal gas equation of state, assuming the specific heat ratio γ equal to 5/3.

A proper treatment of heating and cooling would require a better understanding of the disc's dissipative heating processes and radiative cooling in optically thin and thick regimes. As a first approach, a toy-model approximation will be employed instead; we specify a cooling term $\Lambda_{\rm cool}$ proportional to the viscous and Ohmic heating terms, namely

$$\Lambda_{\rm cool} = f_m Q_{\rm Ohm} + f_u Q_{\rm visc}, \tag{8}$$

Downloaded from http://mnras.oxfordjournals.org/ at Uni Torino Dip Sanità Pubblica Microbiologia on February 19, 2013

where $Q_{\rm Ohm} \propto \eta_m \boldsymbol{J}^2$ and $Q_{\rm visc} \propto \nabla \cdot (\boldsymbol{u} \cdot \Pi) - \boldsymbol{u} \cdot (\nabla \cdot \Pi)$. The non-dimensional parameters f_m and f_u essentially control how much of the entropy increase due to Ohmic and viscous heating, respectively, remains inside the disc. This approach is similar to the one employed in Narayan & Yi (1995) and Casse & Ferreira (2000b), albeit the parametrization is done on the fraction of the actual cooling (Λ) and heating (Q) terms as opposed to their volume integrals. Even though this is still a crude approximation, it allows us to overcome the usual constraint of an adiabatic disc evolution.

2.1 Model description

The initial configuration at $t = 0$ assumes a geometrically thin accretion disc that rotates at a slightly sub-Keplerian velocity around a generic central attractor. The disc, in pressure equilibrium with a radially stratified atmosphere, is threaded by a magnetic field that exits its surface at some angle. We shall take advantage of the system's symmetries, i.e. axial symmetry on the rotation axis (z-axis) and equatorial symmetry at the equator (r-axis). This not only allows us to utilize a two-dimensional approach with three vector components but also reduces computational costs, as we only need to simulate a section of the disc (1/4 of the actual physical extension of the system).

With that in mind the procedure to assign the initial condition in the computational domain, in terms of the primitive variables ($\boldsymbol{V}$), follows the steps of Tzeferacos et al. (2009). In brief and for the sake of clarity they are repeated here.

We begin by specifying a magnetic field configuration via its flux function, ensuring a divergence-free condition throughout the domain. A radially self-similar profile is chosen of the type

$$\Psi = \frac{4}{3} B_{z0} r_0^2 \left(\frac{r}{r_0}\right)^{3/4} \frac{m^{5/4}}{(m^2 + z^2/r^2)^{5/8}}. \tag{9}$$

The components of the magnetic field are then written as

$$B_z = \frac{1}{r}\frac{\partial \Psi}{\partial r}, \qquad B_r = -\frac{1}{r}\frac{\partial \Psi}{\partial z}. \tag{10}$$

The parameter m determines the initial bending of the magnetic field lines whereas the coefficients B_{z0} and r_0 are constants. In our formulation, we use the magnetization parameter $\mu = B^2/2P$ to define the strength of the magnetic field, included in B_{z0}.

The remaining components of $\boldsymbol{V}$ are derived sequentially, starting from a radial self-similarity assumption for density at the equator. Coupling that with a polytropic equation of state (with the polytropic index $\gamma = 5/3$), we derive the equatorial thermal pressure and solve numerically for force equilibrium (in both radial and vertical directions) to obtain the velocity components.

The resulting physical quantities, V_i, follow power laws that for $z = 0$ are of the form

$$V_i = V_{i,0} \left(\frac{r}{r_0}\right)^{\beta_{V_i}}, \tag{11}$$

where β_{V_i} defines the scaling. The power-law coefficients β_{V_i} are $-1/2$ for the three components of the flow speed (the scaling of the Keplerian velocity), $-5/4$ for the components of the magnetic field, $-5/2$ for the gas pressure and $-3/2$ for the density. With this choice the radial dependence for the mid-plane temperature will in turn follow a scaling of r^{-1}.

Above the disc we impose a radially stratified atmosphere, initially in hydrostatic equilibrium; the density and pressure profiles for the atmosphere are

$$\rho_a = \rho_{a0} \left(\frac{1}{\sqrt{r^2 + z^2}}\right)^{1/\gamma - 1}, \quad P_a = P_{a0} \left(\frac{\rho_a}{\rho_{a0}}\right)^{\gamma}. \tag{12}$$

The constant ρ_{a0} is the density of the atmosphere at $R = r_0$, which is assumed to be δ times lighter than the disc's fiducial density ρ_0, i.e. $\rho_{a0} = \delta \rho_0$. The temperature of the corona will then scale with the spherical radius $R = \sqrt{r^2 + z^2}$ as $1/R$. The equilibrium region between the atmospheric and disc pressures defines the disc's initial surface.

The normal collisional diffusion processes inside the disc are always negligible with respect to advection, characterized by a large Reynolds number. Nonetheless, disc instabilities can be triggered and lead to a turbulent state. In such a state, transport coefficients are enhanced during the non-linear evolution of turbulence, leading to anomalous magnetic diffusivity and viscosity that can transport both angular momentum and magnetic field. Even though a conclusive answer regarding the origin of such turbulence is yet to be given, recent studies revealed the existence of a great variety of unstable modes, both in weakly magnetized and equipartition accretion discs (Keppens, Casse & Goedbloed 2002). Instabilities such as the magnetorotational instability (Balbus & Hawley 1991) or the trans-slow Alfvén continuum modes (Goedbloed et al. 2004) are excellent candidates to account for disc turbulence and the associated anomalous transport coefficients in accretion flows. The latter have also the added advantage that they operate with equipartition magnetic fields, which are needed for stationary outflows (Ferreira 1997; Tzeferacos et al. 2009).

On the basis of these arguments we assume that the disc transport coefficients can be modelled in terms of an alpha prescription, as initially proposed by Shakura & Sunyaev (1973). We define two diagonal tensors η_u and η_m, for turbulent viscosity and resistivity. The non-zero components for the viscous coefficient tensor are equal (isotropic behaviour) and given by

$$\eta_u = \alpha_u c_s H \exp\left(-2\frac{z^2}{H^2}\right). \tag{13}$$

Here α_u is the viscosity parameter, while c_s is the sound speed and $H = c_s/\Omega_K = \epsilon\, r$ defines the disc's thermal height scale, both evaluated at the equator. The non-dimensional parameter ϵ is the sound-to-Keplerian speed ratio. The exponential decay ensures that above the disc region transport is negligible and that the ideal MHD formulation applies. Resistivity on the other hand is described by an anisotropic tensor $\eta_{mi,j}$, whose non-zero components are $\eta_{m\phi,\phi} = \eta_m$ and $\eta_{mr,r} = \eta_{mz,z} = \eta_m'$, given by

$$\eta_m = \alpha_m V_{\rm A} H \exp\left(-2\frac{z^2}{H^2}\right). \tag{14}$$

Here α_m is the magnetic diffusivity parameter, while $V_{\rm A} = B_z/\sqrt{\rho}$ is the Alfvén speed at the equator. η_m' is defined through the anisotropy parameter $\chi_m = \eta_m'/\eta_m$.

The two transport coefficients are related through the magnetic Prandtl number, defined at the equator as

$$\mathcal{P}_m = \left.\frac{\eta_u}{\eta_m}\right|_{z=0}. \tag{15}$$

2.2 Parameters and normalization

Our viscous and resistive model has, in total, nine free non-dimensional parameters. Using the notation adopted in the previous

Downloaded from http://mnras.oxfordjournals.org/ at Uni Torino Dip Sanità Pubblica Microbiologia on February 19, 2013

section, these are

(i) ϵ, the sound-to-Keplerian speed ratio $c_s/V_{\rm K}$;
(ii) μ, the magnetization $B^2/2P$, the inverse of plasma β;
(iii) m, an auxiliary parameter controlling the field inclination;
(iv) α_m, the magnetic diffusivity parameter;
(v) χ_m, the anisotropy parameter η_m'/η_m;
(vi) δ, the corona-to-disc density ratio ρ_{a0}/ρ_0;
(vii) $\mathcal{P}_m$, the magnetic Prandtl number;
(viii-ix) f_m, f_u, parameters that control disc cooling via equation (8).

All of the above parametric quantities are subject to constraints and serve to control the initial configuration. According to Ferreira (1997), a trans-Alfvénic solution requires a minimum value for ϵ of 5×10^{-4}. In order to maximize the number of cells in the disc region while retaining a geometrically thin initial disc, we choose $\epsilon = 0.1$.

From our previous investigations, we have established that the initial magnetization is a crucial parameter for the disc–jet system evolution (Tzeferacos et al. 2009). Efficient acceleration and stationary numerical solutions can only be found for μ close to and below equipartition, also in agreement with the analytical studies of Ferreira & Pelletier (1995) and Ferreira (1997) regarding the disc structure.

The bending of the field lines, on the other hand, is dictated by m; a proper choice of its value can reduce currents and forces in the corona. As a convenient side effect, the Blandford & Payne criterion can also be satisfied; such a configuration favours an early onset of the magnetocentrifugal drive. In all runs we set $m = 0.4$ but the field inclination is allowed to change during integration. This, in conjunction with a light corona (δ is set 10^{-4} corresponding to a corona much lighter than the underlying accretion disc), also allows for large characteristic velocities in the propagation of transient features, such as an initial torsional Alfvén wave.

Given the definition of the transport coefficients we can easily see that

$$\eta_u = (\alpha_u c_s H)\Big|_{z=0} \exp\left(-2\frac{z^2}{H^2}\right),$$

$$\eta_m = (\alpha_m V_{\rm A} H)\Big|_{z=0} \exp\left(-2\frac{z^2}{H^2}\right) \rightarrow \mathcal{P}_m = \frac{\eta_u}{\eta_m}\Big|_{z=0} = \frac{\alpha_u c_s}{\alpha_m V_{\rm A}}\Big|_{z=0}$$

$$\rightarrow \alpha_u = \mathcal{P}_m \frac{\alpha_m V_{\rm A}}{c_s}\Big|_{z=0} = \mathcal{P}_m \alpha_m \sqrt{\frac{2\mu}{\gamma}}\,.$$

Therefore, the choice of the viscosity parameter α_u is already imposed by the magnetic Prandtl number $\mathcal{P}_m$. The latter is expected to be of the order of unity in the case of fully developed turbulence (see also Lesur & Longaretti 2009).

The disc's cooling is controlled by f_m and f_u via equation (8) and the energy equation (equation 4). As expected, those parameters must be in the range $(0, 1)$, meaning that for $f_m = f_u = 0$ we obtain solutions where all generated entropy is dissipated inside the accretion disc (analogous to a radiatively inefficient regime; e.g. Casse & Keppens 2004), while for $f_m = f_u = 1$ the solutions are 'cold' and adiabatic, though they include viscosity and resistivity in the disc's dynamics through the momentum and induction equations. The cases studied by varying the values of f_m,f_u are denoted as '$f_m\#f_u\#$'. In this notation, # stands for the fraction of entropy extracted. It is also useful to define $\langle f\rangle \equiv \bar{f} = (1/2)(f_m + f_u)$ for a more compact representation.

In terms of energetics, our simulations differ from the numerical study of radiatively inefficient jet launching by Casse & Keppens (2004) in the following aspects. (i) The parameter $\bar{f}$ allows for more degrees of freedom in the radiation efficiency, even though it is still a crude modelling of cooling to be refined in forthcoming studies. (ii) Heating inside the accretion disc is a result of both anomalous resistivity and viscosity. (iii) The alpha prescription of turbulence in our case specifies $\alpha_m \sim 1$, a requirement for a stationary jet-emitting disc (Ferreira & Pelletier 1995; Ferreira 1997; Combet & Ferreira 2008). The value is 10 times larger than Casse & Keppens (2004, see also Zanni et al. 2007), which unavoidably also affects the Ohmic heating as $Q_{\rm Ohm} \propto \alpha_m$. The values of the parameters are resumed in Table 1.

Table 1. Parameters.

	$f_{m0}f_{u0}$	$f_{m0.2}f_{u0.2}$	$f_{m0.4}f_{u0.4}$	$f_{m0.6}f_{u0.6}$	$f_{m0.8}f_{u0.8}$	$f_{m1}f_{u1}$
f_m	0.0	0.2	0.4	0.6	0.8	1.0
f_u	0.0	0.2	0.4	0.6	0.8	1.0
$\mathcal{P}_m$	1.0	1.0	1.0	1.0	1.0	1.0
μ	0.3	0.3	0.3	0.3	0.3	0.3
α_m	1.0	1.0	1.0	1.0	1.0	1.0
χ_m	3.0	3.0	3.0	3.0	3.0	3.0
ϵ	0.1	0.1	0.1	0.1	0.1	0.1
m	0.4	0.4	0.4	0.4	0.4	0.4
δ	10^{-4}	10^{-4}	10^{-4}	10^{-4}	10^{-4}	10^{-4}

The choice of parameters for the cases studied. (f_m, f_u) control the disc's cooling while $\mathcal{P}_m$ is the magnetic Prandtl number, set to unity. μ is the magnetization, α_m the magnetic diffusivity parameter and χ_m the anisotropy parameter for the resistivity tensor. ϵ is the ratio between the isothermal sound speed and the Keplerian velocity, m the parameter that controls the initial bending of the B field (see equation 10) and δ the corona-to-disc density ratio.

All primitive variables are conveniently normalized to avoid numerical integration of values that may differ quantitatively by many orders of magnitude. The fiducial values are selected so that the resulting scales can efficiently describe the problem. With this in mind, all lengths are normalized to the inner radius of the disc, $r = r_{\rm in} = r_0$ and speeds to the Keplerian velocity calculated at r_0. This choice dictates a time unit equal to $t_0 = r_0/V_{\rm K0}$. Density is normalized with respect to the initial density ρ_0 at the disc's mid-plane and at the inner radius. From the equation of state the resulting P_0 will be equal to ϵ^2, whereas from the momentum equation we get $B_0 = B_{z0} = \epsilon\sqrt{2\mu}$. As a quick reference, the corresponding units in YSO and AGN disc–jet systems are given as follows:

$$r_0 = 0.1\,{\rm au}\ ({\rm YSO})$$
$$= 10\,R_{\rm Schw} = 10^{-4}\left(\frac{M}{10^8\,{\rm M}_\odot}\right)\ {\rm pc}\quad ({\rm AGN}), \tag{16}$$

where $R_{\rm Schw} = 2GM/c^2$ is the Schwarzschild radius of the AGN. The Keplerian velocity will be

$$V_{\rm K0} = 94\left(\frac{M}{{\rm M}_\odot}\right)^{\frac{1}{2}}\left(\frac{r_0}{0.1\,{\rm au}}\right)^{-\frac{1}{2}}\ {\rm km\ s^{-1}}\qquad ({\rm YSO})$$
$$= 6.7\times10^4\left(\frac{r_0}{10\,R_{\rm Schw}}\right)^{-\frac{1}{2}}\ {\rm km\ s^{-1}}\qquad ({\rm AGN}). \tag{17}$$

Given this scaling, the rotation period of the inner disc radius will be 2π, and since $t_0 = r_0/V_{\rm K0}$, the time unit will be

$$t_0 = 1.7\left(\frac{M}{{\rm M}_\odot}\right)^{-\frac{1}{2}}\left(\frac{r_0}{0.1\,{\rm au}}\right)^{\frac{3}{2}}\ {\rm d}\qquad ({\rm YSO})$$
$$= 0.5\left(\frac{M}{10^8\,{\rm M}_\odot}\right)\left(\frac{r_0}{10\,R_{\rm Schw}}\right)^{\frac{3}{2}}\ {\rm d}\qquad ({\rm AGN}). \tag{18}$$

Downloaded from http://mnras.oxfordjournals.org/ at Uni Torino Dip Sanità Pubblica Microbiologia on February 19, 2013

Density is normalized through the choice of a suitable mass accretion rate $\dot{M}_0 = r_0^2 \rho_0 V_{\rm K0}$,

$$\dot{M}_0 = 3 \times 10^{-7} \left(\frac{\rho_0}{10^{-12}\ {\rm g\,cm^{-3}}}\right) \left(\frac{M}{{\rm M}_\odot}\right)^{\frac{1}{2}} \left(\frac{r_0}{0.1\ {\rm au}}\right)^{\frac{3}{2}} {\rm M}_\odot\ {\rm yr}^{-1}$$
$$= 9 \left(\frac{\rho_0}{10^{-12}\ {\rm g\,cm^{-3}}}\right) \left(\frac{M}{10^8\,{\rm M}_\odot}\right)^{2} \left(\frac{r_0}{10\,R_{\rm Schw}}\right)^{\frac{3}{2}} {\rm M}_\odot\ {\rm yr}^{-1}. \quad (19)$$

Having defined the initial thermal height scale through the ϵ parameter, the normalization value for temperature in the mid-plane will be given by $T_{z=0} = \epsilon^2 \frac{m_p G M}{K r}$,

$$T_{z=0} = 10^4 \left(\frac{\epsilon}{0.1}\right)^2 \left(\frac{M}{{\rm M}_\odot}\right) \left(\frac{r}{0.1\ {\rm au}}\right)^{-1} {\rm K} \qquad ({\rm YSO})$$
$$= 5 \times 10^9 \left(\frac{\epsilon}{0.1}\right)^2 \left(\frac{r}{10\,R_{\rm Schw}}\right)^{-1} {\rm K} \qquad ({\rm AGN}). \quad (20)$$

On the other hand, the strength of the poloidal magnetic field at the equator $B_{z=0} = \sqrt{\mu\, 8\pi\, P}$ reads in gauss,

$$B_0 = 2.6 \left(\frac{\mu}{0.3}\right)^{\frac{1}{2}} \left(\frac{\epsilon}{0.1}\right) \left(\frac{M}{{\rm M}_\odot}\right)^{\frac{1}{2}} \left(\frac{\rho_0}{10^{-12}\ {\rm g\,cm^{-3}}}\right)^{\frac{1}{2}} \left(\frac{r}{0.1\ {\rm au}}\right)^{-\frac{5}{4}}$$
$$= 1.8 \times 10^3 \left(\frac{\mu}{0.3}\right)^{\frac{1}{2}} \left(\frac{\epsilon}{0.1}\right) \left(\frac{\rho_0}{10^{-12}\ {\rm g\,cm^{-3}}}\right)^{\frac{1}{2}} \left(\frac{r}{10\,R_{\rm Schw}}\right)^{-\frac{5}{4}}. \quad (21)$$

2.3 Numerical setup

Numerical integration of the MHD equations is carried out using the finite volume/finite difference, shock capturing numerical code PLUTO (Mignone et al. 2007; Mignone, Tzeferacos & Bodo 2010). The computational domain consists of a rectangular region, resolved on to [512 × 1536] cells and spanning in the radial direction from 0 to $40\,r_0$ whereas in the vertical direction (aligned with the rotation axis of the accretion disc) from 0 to $120\,r_0$.

Temporal integration is carried out for 400 time units t_0, using a second-order Runge–Kutta method. Given the normalization described previously and the differential rotation profile, this translates to approximately 63 disc rotations at the inner radius ($r = r_0$), whereas the outer part ($r = 40\,r_0$) has only performed ∼1/4 revolutions. This inconvenient disparity, inherent in such simulations, will limit our search for a stationary outflow in the innermost part of the accretion disc.

Spatial reconstruction is done utilizing a linear interpolation, applying a van Leer limiter for all primitive variables. Upwind fluxes are computed with a Harten–Lax–van Leer Riemann solver.

The upwind constrained transport (UCT) scheme (Londrillo & Del Zanna 2004) is chosen to handle the induction equation for the magnetic field and maintain solenoidality ($\nabla \cdot \boldsymbol{B} = 0$) at machine accuracy.

The initial condition of our runs is displayed in Fig. 1. At the borders of the computational box we still need to specify boundary conditions for the components of $\boldsymbol{V}$. Regions I and II exploit the system's symmetries, i.e. axial symmetry for the rotation axis ($r = 0$, I) and equatorial symmetry at the disc's mid-plane ($z = 0$, II). On the right boundary of the domain ($r = 40\,r_0$, III) we specify an outflow (zero-gradient) condition for density, thermal pressure and the poloidal components of the velocity vector. For the components u_ϕ, B_z and B_ϕ, we retain the first derivative so as to avoid artificial

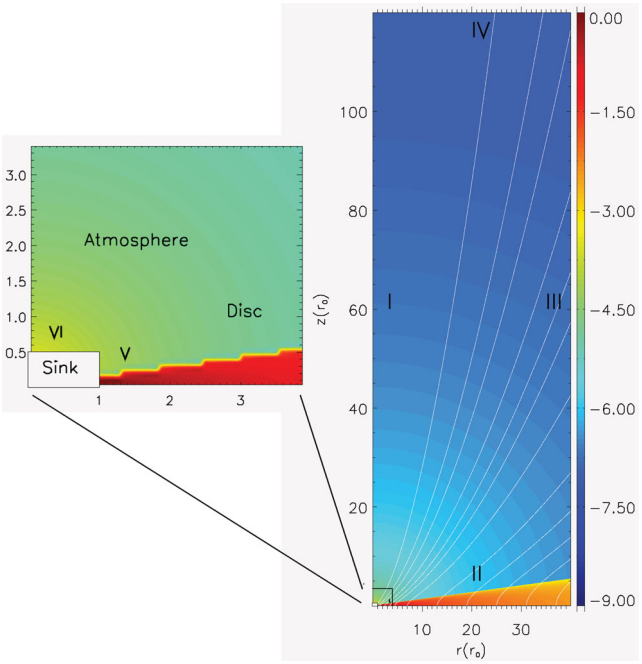

Figure 1. The initial condition, $t = 0$, displaying density logarithm along with sample field lines. The sink/internal boundary region is included as a magnification on the left. Roman numerals denote the six boundary regions, four (I–IV) for the computational domain and two more (V, VI) for the sink.

collimation (see also Ustyugova et al. 1999); B_r is handled by the UCT scheme to ensure solenoidality. On the upper boundary ($z = 120\,r_0$, IV), since no pronounced reflection effects are observed, an outflow condition is imposed for all variables. The normal component of the magnetic field, this time B_z, is once again computed retaining $\nabla \cdot \boldsymbol{B} = 0$.

A specific treatment is needed for the sink region, i.e. where the central attractor is located. Since the star/black hole–disc interaction is beyond the scope of this study and the initial radial self-similar slope is singular for $r = 0$, the origin is excluded from the computational domain. This is accomplished by introducing a rectangular region [$r_0 \times 0.5\,r_0$], inside of which the equations are not evolved. The borders of this internal boundary region, nonetheless, will interact with the system's evolution and are to be treated as ghost zones (V, VI). In this context, we follow the strategy used for regions III and IV, albeit with an additional restriction so as to emulate the sink properties: the poloidal velocity components are required to be less than zero, avoiding thus artefact outflows. The boundary conditions are resumed in Table 2.

3 'WARM' AND 'COLD' OUTFLOWS

Our model is evolved in time for 400 time units, roughly translated into ∼63 rotations at the inner radius. As a reminder, 'warm' cases are those denoted by values of $\bar{f}$, f_m, f_u close to zero, whereas 'cold' cases have these factors close to unity. Due to the favourable initial conditions, we observe the prompt creation of outflows for all values of $\bar{f}$; the ejecta follow the propagation of an initial torsional Alfvén wave, present due to the differential rotation between the atmosphere and the rotating disc (see also Ouyed & Pudritz 1997).

After approximately 10 revolutions of the inner edge of the accretion disc, cases with $\bar{f} \to 1$ have almost reached the upper part of the computational domain (right-hand panels of Fig. 2), while warmer configurations present slower propagation speeds and are

Downloaded from http://mnras.oxfordjournals.org/ at Uni Torino Dip Sanità Pubblica Microbiologia on February 19, 2013

Table 2. Boundary conditions.

V/region	I	II	III	IV	V	VI
ρ	$+V$	$+V$	$\partial_r V = 0$	$\partial_z V = 0$	$\partial_r V = 0$	$\partial_z V = 0$
u_r	$-V$	$+V$	$\partial_r V = 0$	$\partial_z V = 0$	$\partial_r V = 0$	$\partial_z V = 0$
u_ϕ	$-V$	$+V$	$\partial_r^2 V = 0$	$\partial_z V = 0$	$\partial_r^2 V = 0$	$\partial_z V = 0$
u_z	$+V$	$-V$	$\partial_r V = 0$	$\partial_z V = 0$	$\partial_r V = 0$	$\partial_z V = 0$
B_r	$-V$	$-V$	$\nabla \cdot \boldsymbol{B} = 0$	$\partial_z V = 0$	$\nabla \cdot \boldsymbol{B} = 0$	$\partial_z V = 0$
B_ϕ	$-V$	$-V$	$\partial_r^2 V = 0$	$\partial_z V = 0$	$\partial_r^2 V = 0$	$\partial_z V = 0$
B_z	$+V$	$+V$	$\partial_r^2 V = 0$	$\nabla \cdot \boldsymbol{B} = 0$	$\partial_r^2 V = 0$	$\nabla \cdot \boldsymbol{B} = 0$
P	$+V$	$+V$	$\partial_r V = 0$	$\partial_z V = 0$	$\partial_r V = 0$	$\partial_z V = 0$

Boundary conditions of the computational box and the sink region (see Fig. 1), for all primitive variables ($\boldsymbol{V}$). For the symmetry regions I and II, the ghost cell values of the V component of $\boldsymbol{V}$ are specified via symmetric ($+V$) and antisymmetric ($-V$) reflections of their respective values inside the computational domain. For the remaining ghost zone regions (III–VI), we utilize either outflow or constant first derivative conditions, depending on the variable (see the text). Normal (with respect to the boundary) components of the magnetic field are computed by the UCT scheme to impose $\nabla \cdot \boldsymbol{B} = 0$. Furthermore, the poloidal components of velocity for regions V and VI are required to be less than zero, preventing artefact outflows from the sink.

considerably denser (left-hand panels of Fig. 2). In all six simulations discussed, we obtain current-carrying outflows in agreement with the analytical results of Ferreira (1997) and Casse & Ferreira (2000b).

The long-term evolution of the flow and the poloidal magnetic field is seen in Fig. 3 where two extreme cases are presented, namely $f_m0.2\,f_u0.2$ and $f_m0.8\,f_u0.8$. The most pronounced difference is in the jet density: warmer cases can be as much as two to three times denser than colder ones.

The resulting field topology is similar if projected on the poloidal plane but differs in pitch: the ratio of toroidal to poloidal fields B_ϕ/B_p is larger for colder cases. This occurs due to a relatively slower rotation rate of the accretion disc at the innermost radii for warmer cases. As a result, the winding of the magnetic field lines is less pronounced but still helical.

The jet acceleration can be monitored through the flow's terminal velocity. In Fig. 4 we show the ratio of poloidal to Keplerian speeds, the latter calculated at $z = 0$, along a selected field line. The range of the obtained velocities is quite large: dense and 'warm' flows have speeds near the Keplerian, while for 'cold' flows we reproduce the results shown in fig. 8 of Tzeferacos et al. (2009). Denoted along the field line, the letters 'A' and 'F' show the locus of the Alfvén and fast critical points, respectively. The Alfvén point is crossed at lower altitudes in warmer cases, confirming Casse & Ferreira (2000b).

In order to examine the acceleration mechanism's properties, it is useful to analyse the forces at play and the sequence of events. Matter is deflected from accretion by thermal pressure gradients (the only non-pinching force inside the accretion disc), leaves the viscous/resistive regime and is loaded on to the field lines. Due to differential rotation, the initially poloidal magnetic field generates a toroidal component (see also Fig. 3).

The flow's dynamics are subject to the forces resumed in Fig. 5 for an intermediate case $f_m0.6f_u0.6$. The upper panel displays the force components *along* a given magnetic field line situated at $r = 1.5\,r_0$ after ∼63 rotations. In the sub-Alfvénic region, the dominant driving force is the centrifugal one, whereas at greater heights over the disc the Lorentz force is responsible for the acceleration, mainly through the magnetic pressure gradient of B_ϕ. This two-part drive is the magnetocentrifugal acceleration discussed by Blandford & Payne (1982). It should be noted that thermal pressure gradients are important only in the base of the outflow, albeit their contribution to the drive becomes more important for small $\bar{f}$. Magnetic and centrifugal forces are also dominant in the trans-field balance (lower panel of Fig. 5). The magnetic surface is subject to the decollimating centrifugal force and the confining (since the footpoint is located at a small disc radius) magnetic force, with the hoop stress being prevalent.

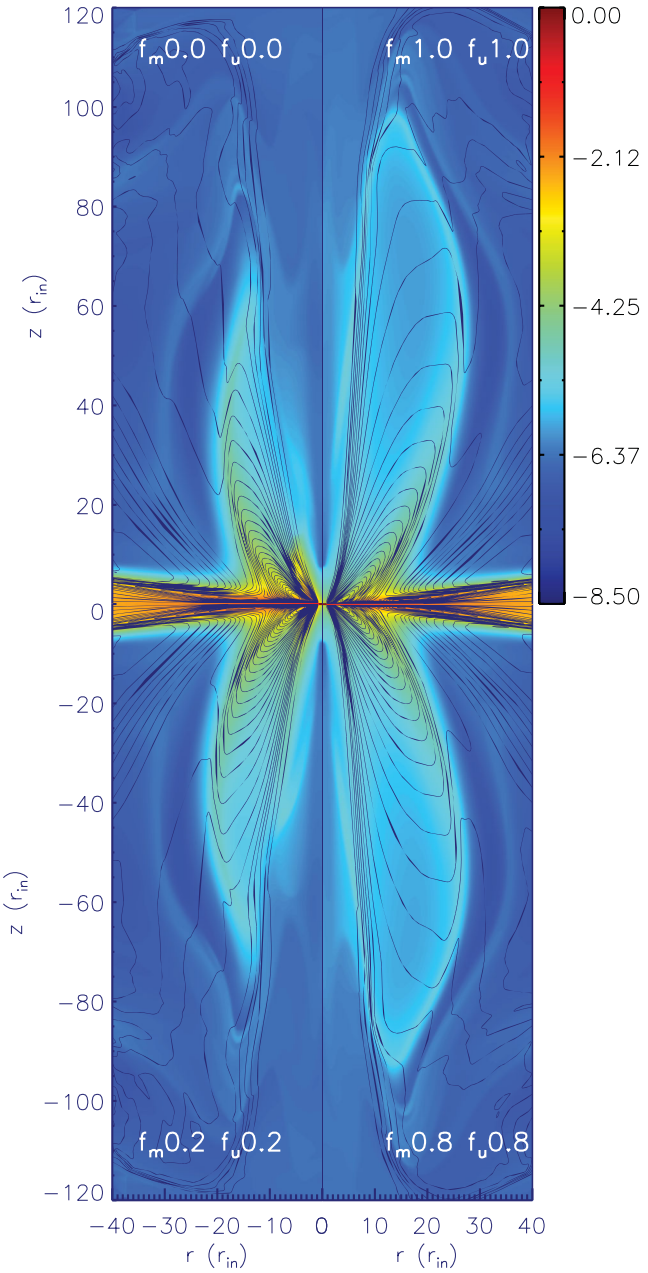

Figure 2. Four snapshots of the poloidal current distribution and logarithmic density after ∼10 inner radius rotations. The extreme cases ('warm' on the left, 'cold' on the right) are displayed. All present a 'butterfly' current configuration, but the expansion of the initial torsional Alfvén wave and the outflow that follows are faster for colder solutions. For values of $\bar{f}$ close to zero, the resulting outflow is slower and denser.

The efficiency of the accelerating mechanism is linked to the transformation of magnetic energy into kinetic energy. For every

Downloaded from http://mnras.oxfordjournals.org/ at Uni Torino Dip Sanità Pubblica Microbiologia on February 19, 2013

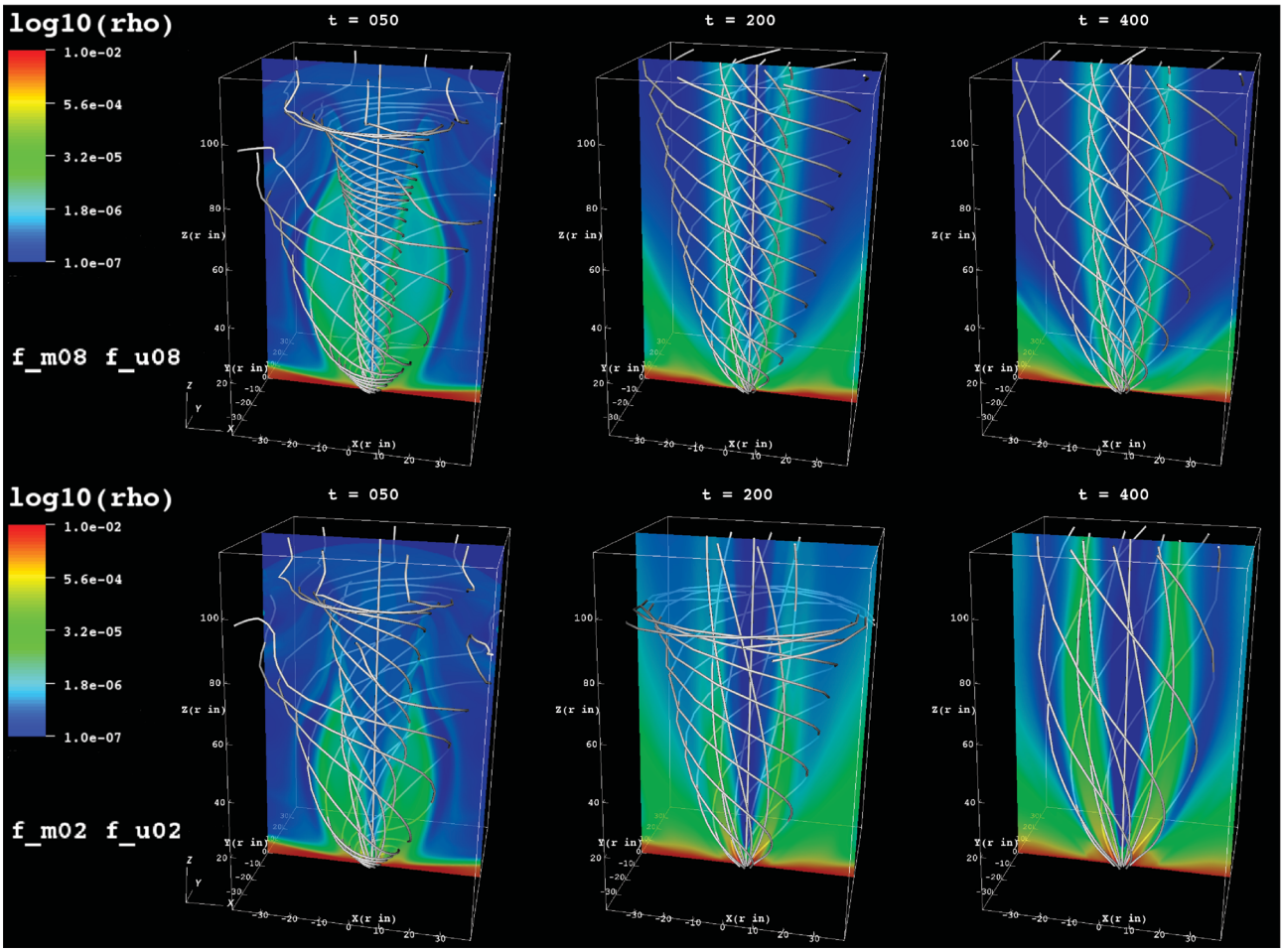

Figure 3. Evolution of the density logarithm and sample magnetic field for cases $f_m0.8f_u0.8$ ('cold', upper part) and $f_m0.2f_u0.2$ ('warm', lower part). The two-dimensional solution is rendered on to a three-dimensional Cartesian grid to follow also the evolution of the toroidal magnetic field.

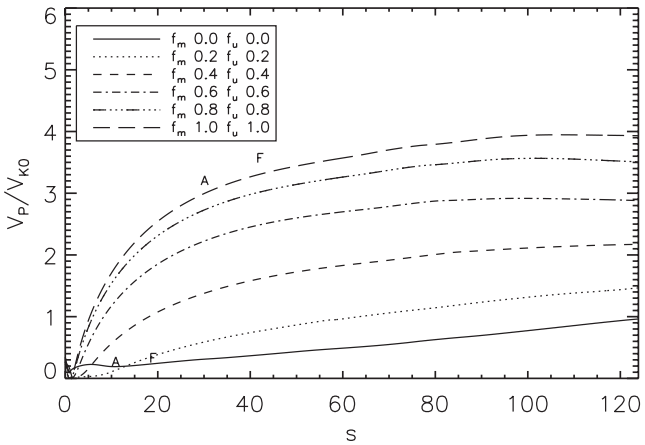

Figure 4. Poloidal velocity along a field line whose footpoint is anchored at $r = 2\,r_0$ and normalized over the Keplerian speed at the footpoint, at time $t = 400$. Warmer cases are notably slower, with terminal velocities close to the Keplerian.

case, we evaluate the Poynting-to-kinetic flux ratio

$$\sigma = \frac{-2\Omega r B_\phi B_p}{\rho u^2 u_p} \tag{22}$$

along a fiducial field line and report in the upper panel of Fig. 6 its asymptotic value, as found at the upper part of the computational box. Here Ω denotes the rotation rate of the magnetic surface (an integral of motion). As $\bar{f}$ increases, moving from 'warm' to 'cold' outflow solutions, the asymptotic value of σ decreases. This implies that the magnetic energy not yet transformed is larger for warmer cases, agreeing with the trend shown in the poloidal velocity.

Note that for all cases a trans-Alfvénic flow is observed. The usual analytical condition for that, in stationary 'cold' outflows, requires

$$\omega_{\rm A} = \frac{\Omega r_{\rm A}}{V_{\rm Ap,A}} > 1, \tag{23}$$

where $r_{\rm A}$ is the Alfvén radius and $V_{\rm Ap,A}$ the poloidal component of the Alfvén speed at the Alfvén point. The $\omega_{\rm A}$ is called the fastness parameter and distinguishes jets in 'fast' ($\omega_{\rm A} > 1$) and 'slow' ($\omega_{\rm A} < 1$) rotators (Michel 1969; Pelletier & Pudritz 1992; Ferreira 1997). The condition of equation (23), nonetheless, applies only for solutions with very large magnetic lever arms (equation 28). In Casse & Ferreira (2000b) a generalized condition is described that allows for super-Alfvénic flows even for values of $\omega_{\rm A}$ less than unity, i.e. super-Alfvénic slow rotators when the disc's surface is heated. Applying that line of thought in our simulations, we calculate the fastness parameter for a field line rooted at $r = 1.5\,r_0$, for all cases. In the lower panel of Fig. 6 we see that we do obtain slow

Downloaded from http://mnras.oxfordjournals.org/ at Uni Torino Dip Sanità Pubblica Microbiologia on February 19, 2013

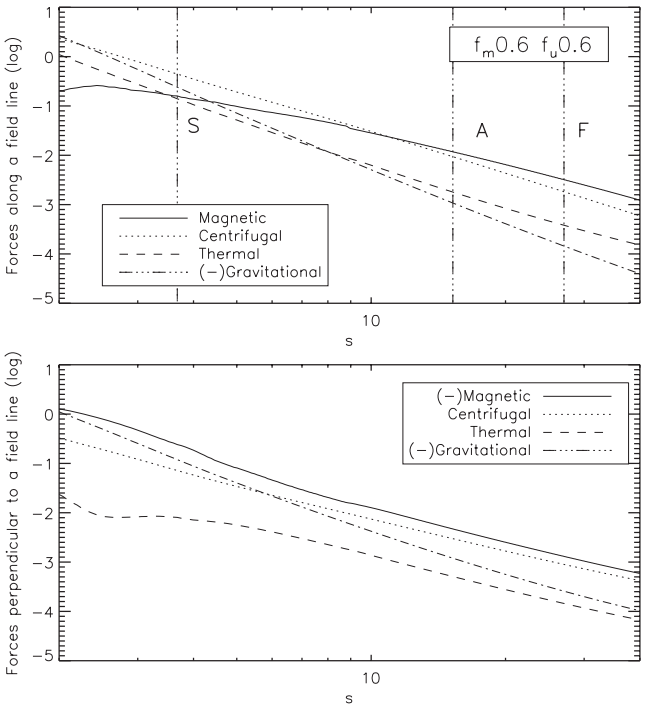

Figure 5. Upper panel: logarithmic magnitude of forces *along* a field line with its footpoint anchored at $r = 2\,r_0$ at time $t = 400$ for case $f_m 0.6 f_u 0.6$. Displayed are the Lorentz (solid), centrifugal (dotted), thermal (dashed) and gravitational (dot–dashed) forces. Forces that in the legend display a $(-)$ in front decelerate the outflow. Perpendicular lines, noted as 'S', 'A' and 'F', show the locus of the slow, Alfvén and fast critical points, respectively. Lower panel: logarithmic magnitude of forces *perpendicular* to the same field line. Forces that in the legend display a $(-)$ in front collimate the outflow.

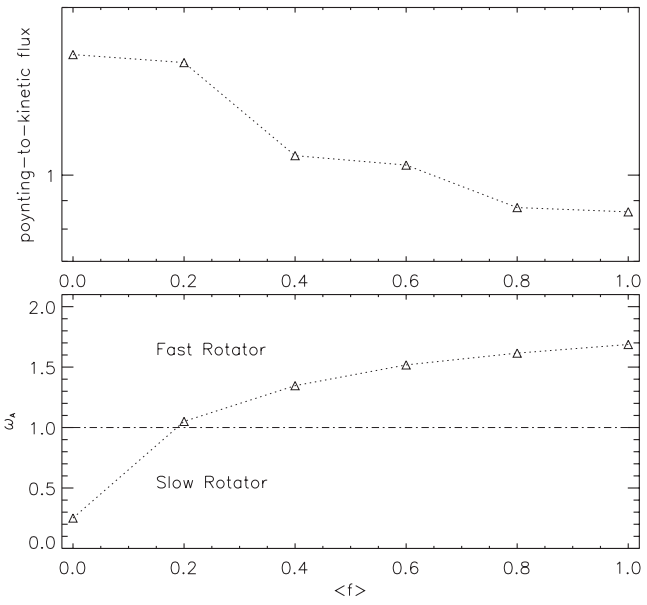

Figure 6. Upper panel: asymptotic Poynting-to-kinetic flux ratio, as a function of $\bar{f}$. For warmer cases the transformation of magnetic energy is less prominent. Lower panel: fastness parameter ω_A, as a function of $\bar{f}$. Even though most cases are fast rotators, we obtain solutions that are super-Alfvénic slow rotators.

rotator solutions for the warmest of cases which cross nevertheless the Alfvén point, confirming the theoretical predictions of Casse & Ferreira (2000b).

4 DISC BEHAVIOUR

Apart from altering the jet dynamics, Ohmic and viscous heating will also modify the accretion disc's structure. We can write the conservation of energy (equation 4) in primitive form such as

$$\frac{\partial T}{\partial t} + \boldsymbol{u}\cdot\nabla T = (\gamma - 1)(Q - T\nabla\cdot\boldsymbol{u}). \tag{24}$$

From this equation we can expect that by allowing for fractions of $Q_{\rm Ohm}$ and $Q_{\rm visc}$ in the net energy per unit mass term Q (upper panel of Fig. 7), (a) the disc temperature will rise (upper panel of Fig. 8) and (b) the vertical thermal pressure gradient will increase (lower panel of Fig. 8), promoting mass ejection. Even though we find a monotonic increase in surface temperature T_+ as $\bar{f}$ decreases, compatible with the results of Casse & Ferreira (2000b), unlike this

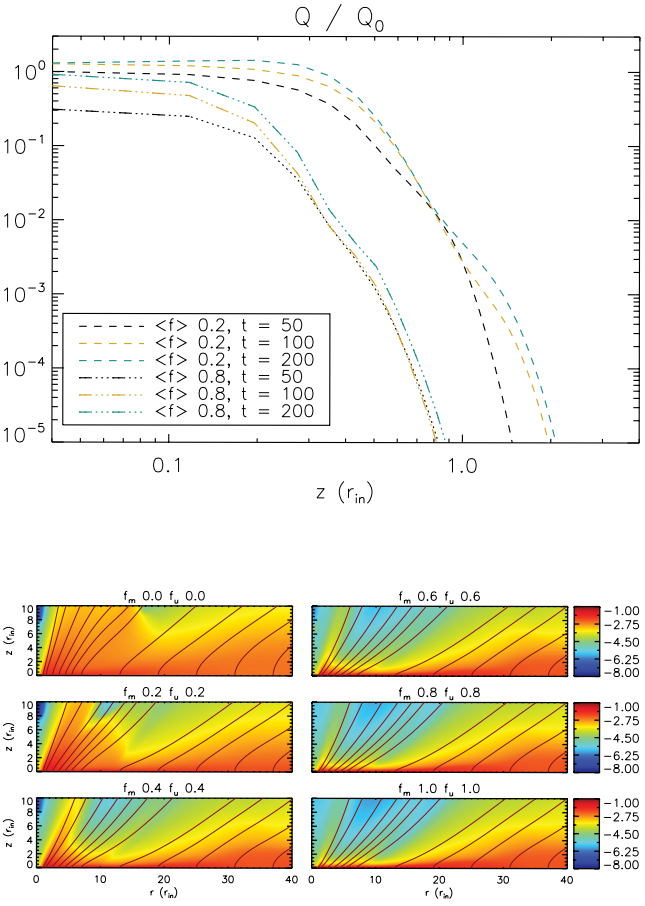

Figure 7. Upper panel: temporal evolution of vertical profiles of Q (sum of the fractions of Ohmic and viscous heating dissipated in the accretion disc) for the cases presented in Fig. 3, at $r = 5\,r_0$. The displayed energy input is normalized to the value of Q for $\bar{f} = 0.2$ at $z = 0$ and $t = 50$ for the sake of exposition. Note that for the warmer case $\bar{f} = 0.2$, Q is not only larger than its 'cold' case ($\bar{f} = 0.8$) equivalent but also retains large values at higher altitudes as the simulation progresses. This significantly enhances mass loading at the disc surface. Lower panel: logarithmic density in the accretion disc region for all cases at the end of the simulations. Also depicted are sample poloidal field lines whose inclination at the surface decreases (straighter lines) as $\bar{f}$ decreases. The disc's geometrical thickness increases for warmer solutions.

Downloaded from http://mnras.oxfordjournals.org/ at Uni Torino Dip Sanità Pubblica Microbiologia on February 19, 2013

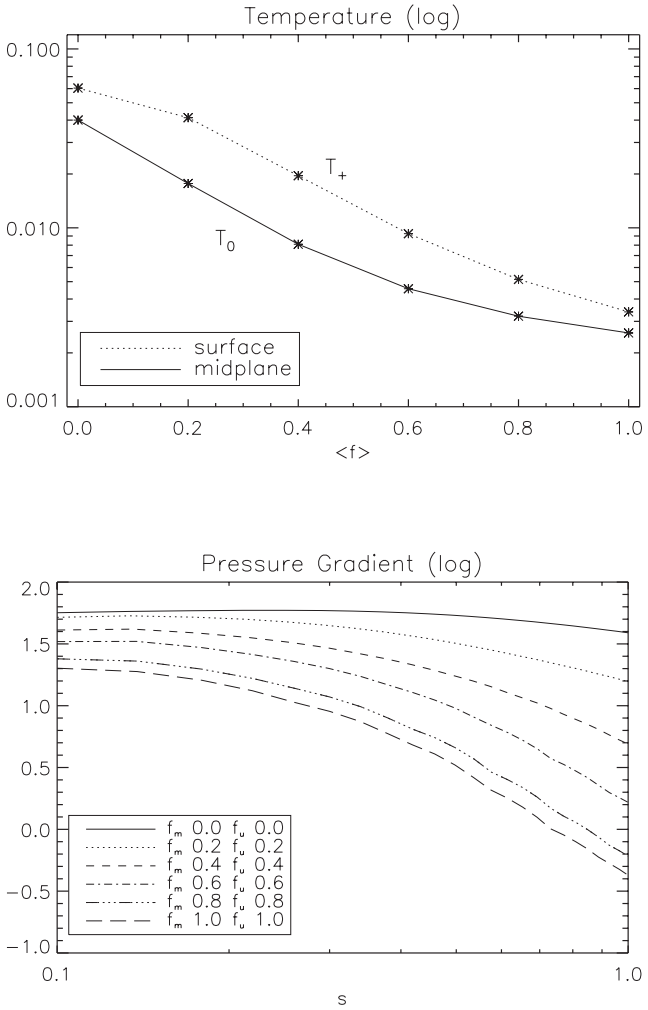

Figure 8. Upper panel: surface and mid-plane mean disc temperatures for all cases in the ejection region, $r \in [1\,r_0, 10\,r_0]$, after ∼63 rotations. Heating effects due to transport coefficients can increase the temperature up to approximately one order of magnitude. Lower panel: thermal pressure gradient *along* a magnetic field line anchored at $r = 5.0\,r_0$. A closeup in the disc region is shown for all cases. Colder cases present smaller values (resulting to less mass being loaded on to the field line) and faster decay, since the disc retains the initial geometrical thickness.

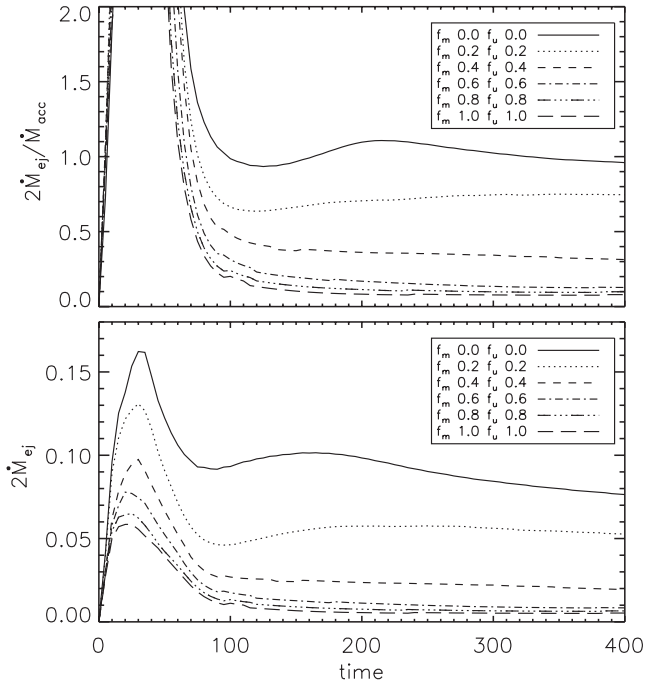

Figure 9. Temporal evolution of the ejection-to-accretion rate (upper panel) and the ejection rate (lower panel) for the cases studied. The increase of entropy inside the accretion disc results in stronger ejection but cases like $f_m 0 f_u 0$ and $f_m 0.2 f_u 0.2$ present ejection-to-accretion rates that are much larger than those observed.

study our heating effects are not a priori localized on the disc's surface but extend throughout the disc structure. This also results in an increase in the mid-plane temperature, T_0, which in turn specifies a new thermal height scale $H(T_0)$ and leads to a geometrically thicker disc. In the upper panel of Fig. 8 we display mean values of surface and mid-plane temperature at the ejection region. Note that, even for 'cold' solutions, the ratio T_+/T_0 remains above unity, a numerical effect due to diffusion at the disc's surface. This limitation has been pointed out before (e.g. Zanni et al. 2007; fig. 12 of Tzeferacos et al. 2009 or the discussion in Murphy et al. 2010).

The impact on the disc's geometry can be seen in the lower panel of Fig. 7, where the density logarithm of the disc for all cases is displayed, along with sample field lines, after ∼63 rotations. As expected, the disc becomes thicker as temperature rises, more prominently in the inner part as it has rotated more. The poloidal magnetic field lines show a decrease in curvature $\mathcal{R}$ and inclination at the surface. As discussed in Ferreira (1997), for 'cold' solutions there is an *inverse* relation between the ejection index and the curvature,

$$\xi = \frac{\ln(1 - 2\dot{M}_{\rm ej}/\dot{M}_{\rm acc})}{\ln(r_i/r_e)}. \tag{25}$$

The same qualitative behaviour exists also in 'warm' analytical solutions, where mass loading is enhanced (larger ξ) and the poloidal lines are straighter (also found in fig. 8 of Casse & Ferreira 2000b and fig. 5 of Ferreira 2002).

A proper treatment of the inflow–outflow dynamics is required to study the impact of Ohmic and viscous heating on the mass loading process. We define a box-like control volume, similarly to Zanni et al. (2007), whose surfaces $S_{\rm i}$, $S_{\rm e}$ reside at $r = r_{\rm i} = 1\,r_0$ and $r = r_{\rm e} = 10\,r_0$, respectively, while surface $S_{\rm d}$ on top of the disc is located at $1.5H$. The mass flux entering the control volume from S_e is given by

$$\dot{M}_{\rm acc} = -2\pi r \int_{-1.5H}^{1.5H} \rho u_r \, {\rm d}z, \tag{26}$$

whereas the mass ejected through the S_d is

$$\dot{M}_{\rm ej} = \int_{S_d} \rho \boldsymbol{u} \cdot {\rm d}\boldsymbol{S}. \tag{27}$$

In Fig. 9 we can see the temporal evolution of the ejection-to-accretion rate (upper panel) and the actual ejection rate (lower panel) as a function of time. It is evident that the disc's heating, by increasing the only non-pinching force ∇P, deflects more matter on to the field lines amplifying ejection rates up to factors of even greater than 10. Nonetheless, accretion-to-ejection rates such as those obtained for $\bar{f} \leq 0.2$ are not observed (∼0.96, 0.75 at the end of integration) and do not reach some plateau to indicate stationarity (in agreement with Zanni et al. 2007).

Downloaded from http://mnras.oxfordjournals.org/ at Uni Torino Dip Sanità Pubblica Microbiologia on February 19, 2013

Table 3. Ejection index, magnetic lever arm (mean value over the control volume) and terminal velocity (at $r = 1.5\,r_0$).

	Plateau	$2\dot{M}_{\rm ej}/\dot{M}_{\rm acc}$	ξ	λ	$V_p/V_{\rm K}$
f_m1f_u1	$\surd$	0.08	0.036	$\sim$15	3.9
$f_m0.8f_u0.8$	$\surd$	0.10	0.046	$\sim$11	3.5
$f_m0.6f_u0.6$	$\surd$	0.13	0.060	$\sim$9	2.9
$f_m0.4f_u0.4$	$\surd$	0.31	0.161	$\sim$4	2.1

Intermediate 'warm' cases however present some astrophysical relevance. For those we calculate the ejection index using equation (25) and obtain the results that are summarized in Table 3. As $\bar{f}$ decreases to warmer configurations, the ejection index ξ increases. The inverse trend is observed for the magnetic lever arm, an MHD invariant along a given field line, defined at the Alfvénic surface as

$$\lambda = \frac{L(A)}{\Omega(A) r_0^2} = \left(\frac{r_{\rm A}}{r_0}\right)^2 . \tag{28}$$

The values reported in Table 3 are found by mediating at different radii in the control volume. The resulting range is between ~ 4 for $\bar{f} = 0.4$ and ~ 15 for $\bar{f} = 1$. Such a range of lever arms and velocities is fairly compatible with the analytical study of Casse & Ferreira (2000b), although their values of λ are comparatively larger at the cold limit; this again can be attributed to numerical diffusion at the disc's surface, which acts as a small additional heating source that promotes mass ejection. The inverse correlation between mass loading and magnetic lever arm, found by many previous investigators (e.g. Blandford & Payne 1982,Ouyed & Pudritz 1997, Ferreira 1997 to name a few), is confirmed.

The analysis of the angular momentum and energy balance of the accretion disc can provide important indications about its properties. In a stationary situation, the angular momentum balance can be written as

$$\dot{J}_{\rm acc} = 2\dot{J}_j + \dot{J}_{\rm vis} , \tag{29}$$

showing that the angular momentum flux due to accretion

$$\dot{J}_{\rm acc} = \int_{S_{\rm i}} (r\rho u_\phi \boldsymbol{u} - r B_\phi \boldsymbol{B})\cdot {\rm d}\boldsymbol{S} - \int_{S_{\rm e}} (r\rho u_\phi \boldsymbol{u} - r B_\phi \boldsymbol{B})\cdot {\rm d}\boldsymbol{S} \tag{30}$$

can be driven by the jet torque

$$\dot{J}_j = \int_{S_d} \left(r\rho u_\phi \boldsymbol{u} - r B_\phi \boldsymbol{B}\right)\cdot {\rm d}\boldsymbol{S} , \tag{31}$$

given by the sum of the kinetic and magnetic fluxes, or the viscous torque

$$\dot{J}_{\rm vis} = \int_{S_{\rm i}} r\boldsymbol{\Pi}\cdot {\rm d}\boldsymbol{S} - \int_{S_{\rm e}} r\boldsymbol{\Pi}\cdot {\rm d}\boldsymbol{S} , \tag{32}$$

where the vector $\boldsymbol{\Pi}$ is responsible for the poloidal transfer of the disc's angular momentum due to viscous stresses and is equal to $(\Pi_{r,\phi}, 0, \Pi_{z,\phi})$.

In a similar manner, the energy balance can be written as

$$\dot{E}_{\rm lib} = \dot{E}_{\rm rad} + \dot{E}_{\rm enth} + 2\dot{E}_j . \tag{33}$$

This equation shows that the energy liberated by accretion between $r_{\rm e}$ and $r_{\rm i}$

$$\dot{E}_{\rm lib} = \int_{S_{\rm i}} \left[\left(\Phi_g + \frac{1}{2}u^2\right)\rho\boldsymbol{u} + \boldsymbol{E}\times\boldsymbol{B} - \boldsymbol{u}\Pi\right]\cdot {\rm d}\boldsymbol{S} - \int_{S_{\rm e}} \left[\left(\Phi_g + \frac{1}{2}u^2\right)\rho\boldsymbol{u} + \boldsymbol{E}\times\boldsymbol{B} - \boldsymbol{u}\Pi\right]\cdot {\rm d}\boldsymbol{S} , \tag{34}$$

Table 4. Angular momentum and energy fluxes at the end of the integration of cases converging towards a steady state.

	$\dot{J}_{\rm vis}/2\dot{J}_j$	$\dot{E}_{\rm rad}/\dot{E}_{\rm lib}$	$\dot{E}_{\rm enth}/\dot{E}_{\rm lib}$	$2\dot{E}_j/\dot{E}_{\rm lib}$
f_m1f_u1	0.04	0.04	0.08	0.87
$f_m0.8f_u0.8$	0.03	0.05	0.10	0.83
$f_m0.6f_u0.6$	0.02	0.04	0.15	0.76
$f_m0.4f_u0.4$	0.05	0.04	0.33	0.58

given by the sum of mechanical, magnetic and viscous powers can be extracted as radiation

$$\dot{E}_{\rm rad} = \int_{V_c} \Lambda_{\rm cool}\,{\rm d}V = \int_{V_c} \bar{f}\,(Q_{\rm visc} + Q_{\rm res})\,{\rm d}V , \tag{35}$$

advected towards the central object by the enthalpy flux

$$\dot{E}_{\rm enth} = \int_{S_{\rm e}} \frac{\gamma\,P}{\gamma - 1}\boldsymbol{u}\cdot {\rm d}\boldsymbol{S} - \int_{S_{\rm i}} \frac{\gamma\,P}{\gamma - 1}\boldsymbol{u}\cdot {\rm d}\boldsymbol{S} , \tag{36}$$

or extracted by the jet

$$\dot{E}_j = \int_{S_d} \left\{\left[\left(\Phi_g + \frac{1}{2}u^2\right)\rho + \frac{\gamma\,P}{\gamma - 1}\right]\boldsymbol{u} + \boldsymbol{E}\times\boldsymbol{B}\right\}\cdot {\rm d}\boldsymbol{S} . \tag{37}$$

The relative weight of the terms on the right-hand side of equations (29) and (33) allows us to distinguish between different disc solutions. For example, in a standard accretion disc (Shakura & Sunyaev 1973), the accretion power (equation 34) fuels the radiative emission of the disc (equation 35), while in an ADAF solution (Narayan & Yi 1995) most of the energy liberated by accretion is advected towards the central object in the form of enthalpy (equation 36). In a disc emitting powerful jets, the outflows extract most of the energy and angular momentum. In Table 4 we present the values of these different terms for the simulations that converge towards a steady state. In the first column we can clearly see that the torque exerted by the jets on to the disc largely dominates the viscous one. Consequently, we verified that the viscous contribution to the accretion power is negligible, as well as the magnetic term: the power released by accretion is essentially given by the mechanical energy. In the second column we show that our solutions are clearly radiatively inefficient with most of the accretion power released in the jet (fourth column). In any case, a trend is clearly visible: as we increase the amount of energy which is dissipated locally inside the disc, the enthalpy accretion flux becomes more and more important at the expenses of the jet power. Cold simulations correspond to a solution where the outflows extract essentially all the energy and angular momentum from a geometrically thin disc, as in the models by Blandford & Payne (1982) or Ferreira (1997). In the simulations characterized by smaller values of the $\bar{f}$ parameter, the outflow is accelerated from a geometrically thicker disc where the disc enthalpy flux becomes of the same order of magnitude as the jet power: this corresponds to a situation closer to the adiabatic inflow-outflow system (ADIOS) models (Blandford & Begelman 1999). Note that since the rotation of a thick disc becomes sub-Keplerian and tends to decrease towards the disc surface, magnetocentrifugal effects only are not efficient enough to launch an outflow from the surface of a thick disc (Ferreira 1997): necessarily, the outflows need an extra pressure term that is provided, in our simulations, by the dissipative heating at the disc surface.

Finally, note that the sum of the energy terms gets close to 1 in colder cases, pointing out that these simulations reach a steady state. As the $\bar{f}$ parameter decreases, the sum departs from 1, marking the

Downloaded from http://mnras.oxfordjournals.org/ at Uni Torino Dip Sanità Pubblica Microbiologia on February 19, 2013

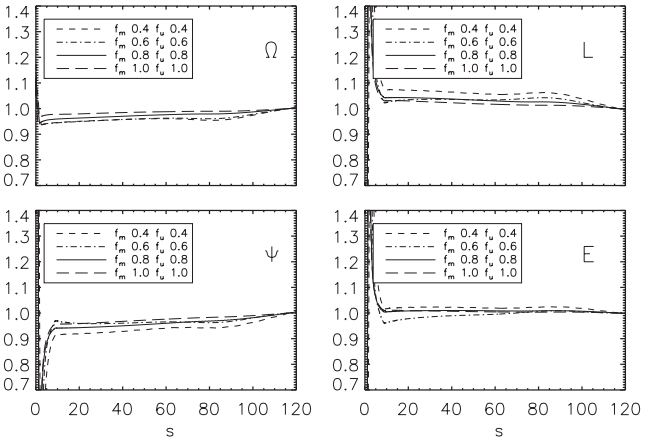

Figure 10. MHD invariants calculated along a magnetic field line at $r = 1.5\,r_0$. The ratio of the invariant over its final value is shown for cases $0.4 \leq \bar{f} \leq 1$. The deviation above the accretion disc remains small: ∼5 per cent.

transition to the non-stationary solutions we obtained for $\bar{f}$ equal to 0 and 0.2.

The stationarity of intermediate 'warm' and 'cold' cases is verified unequivocally through the MHD invariants. MHD axisymmetric analytical models have shown that certain quantities are conserved along any given magnetic surface in steady-state configurations (Tsinganos 1982). In terms of the poloidal magnetic flux $A = 1/2\pi \int \boldsymbol{B}_p \cdot \mathrm{d}\boldsymbol{S}$ of a field line whose footpoint is situated at a radius r, we can write the following integrals:

$$\Psi(A) = \sqrt{4\pi\rho}\frac{V_p}{B_p},$$

$$\Omega(A) = \frac{1}{r}\left(V_\phi - \frac{\Psi(A)B_\phi}{\sqrt{4\pi\rho}}\right), \quad L(A) = r\left(V_\phi - \frac{\sqrt{4\pi}B_\phi}{\Psi(A)}\right),$$

$$E(A) = \frac{V^2}{2} + \frac{\gamma}{\gamma-1}\frac{P}{\rho} + \Phi - r_0\Omega(A)\frac{\sqrt{4\pi}B_\phi}{\Psi(A)}. \qquad (38)$$

In Fig. 10 we display the ratio of each invariant over its final (asymptotic) value, along a fiducial field line at $r = 1.5\,r_0$. Since above the disc the value is close to unity (in the range $\sim 0.95-1.05$), we can safely assume that a quasi-stationary state is reached. Note once more that the deviation from the asymptotic values is more prominent for smaller values of $\bar{f}$, which agrees with the trends seen earlier on the energy budget analysis.

5 DISCUSSION

Our results confirm that thermal effects can alter both the disc-outflow dynamics and disc structure, while also controlling directly the physical properties of the jet. Even though based on a toy model for the cooling function, the present study shows that the mass load (in terms of the amount of mass ejected from the disc) can increase dramatically if large fractions of Ohmic and viscous heating are allowed to raise the disc's enthalpy. This in turn leads to slower, denser outflows. Clearly, a more accurate treatment of the energy equation is required in order to provide reliable diagnostics for the disc's ejection efficiency ξ, including realistic heating, cooling and transport processes. A priori assumptions of the level of turbulence, such as the alpha prescription, are prone to inconsistencies: if the thermal scale height H increases too much (as with case $\bar{f} = 0$ for example), diffusivity (which is strongly correlated with heating as $\eta_m \propto H$) will further enhance thermal effects. We must therefore treat MHD turbulence in a more consistent way.

'Warm' outflows and acceleration. In all cases we obtain the generation of a super-Alfvénic, superfast magnetosonic outflow. However, different configurations lead to different jet densities and velocities. For 'warm' flows the velocities obtained ($\propto V_{\mathrm{K0}}$) are typically slower – by a factor of 3 to 4 (Fig. 4) – than 'cold' solutions. Correspondingly 'cold' flows are two to three times lighter than what is obtained for large entropy generation (Fig. 3). The fastness parameter ω_A was found to reach values close to and below unity for cases of $\bar{f} \leq 0.2$, in agreement with Casse & Ferreira (2000b) who found super-Alfvénic solutions for slow rotators.

Collimation and currents. Regarding the topology of the current loops, which defines the flow's acceleration, no pronounced difference was found: in all cases a butterfly topology was obtained, compatible with analytical predictions (Ferreira 1997). The inclination of the poloidal magnetic field at the disc's surface, on the other hand, was found to decrease (Fig. 7), qualitatively in agrement with Casse & Ferreira (2000b). Even though all cases retain an open poloidal field, the magnetic pitch differs: in large $\bar{f}$ configurations the field winds up more with respect to warmer cases.

Disc–jet connection and mass load. The effects of entropy generation alter the interplay between the accretion disc and the outflow in two ways: (i) the temperature and the geometrical thickness of the disc increase (upper panel of Fig. 8) and (ii) the thermal pressure gradient becomes stronger (lower panel of Fig. 8). The latter is responsible for an enhanced deflection of the accreting plasma on to the magnetic field lines. Fig. 9 shows that Ohmic and viscous heating can increase the ejection rate by factors of larger than 10, while the same is also true for ejection-to-accretion rates. Regarding the disc's energetics, most of the energy liberated by accretion is given by mechanical power, with a negligible viscous contribution. Correspondingly, the accretion power is mainly extracted by the bipolar jets and only a tiny fraction is radiated. Nevertheless, as the amount of turbulent energy dissipated inside the disc increases (i.e. the $\bar{f}$ parameter decreases), the enthalpy flux advected by accretion towards the central object becomes comparable to the jet power, as in the case of ADIOS models.

Stationarity. The flattening of the ejection-to-accretion rates (Fig. 9) and the balance between accretion and jet/radiation powers suggest that a quasi-stationary state is reached for $\bar{f} \geq 0.4$. This is confirmed by the behaviour of flow invariants shown in Fig. 10. Nevertheless, this result applies only for the flow originating from the innermost part of the accretion disc, as the dynamical evolution of the outer part is too limited to permit any conclusion regarding stationarity.

Comparison with disc-wind models from the co-rotation radius. The numerical solutions recovered in this study fall in the category of extended disc winds (see for example fig. 1 a in Ferreira et al. 2006), which place the jet origins at radii that span from the disc's inner radius r_{i} up to an external radius $r_{\mathrm{e}} \gg r_{\mathrm{i}}$. A different paradigm, originally suggested by Shu et al. (1994), is that of disc-powered jets launched from the 'X-region' with $r_{\mathrm{e}} \simeq r_{\mathrm{i}}$ (e.g. figs 3 and 4 in Shu et al. 1994). Such an ejection region has the added benefit of bringing the star–disc dynamics into the picture, allowing for the wind to tap into the angular momentum reservoir of the star and explain naturally its spin-down. Although the launching processes involved are similar to ours, i.e. magnetocentrifugal acceleration for X-winds (Shu et al. 1994) and magnetic drive for conical/propeller-driven winds (Romanova et al. 2009), there exist a number of differences which should be discussed.

Downloaded from http://mnras.oxfordjournals.org/ at Uni Torino Dip Sanità Pubblica Microbiologia on February 19, 2013

A crucial distinction between the two scenarios is the amount of magnetic flux threading the accretion disc (Ferreira et al. 2006). While in the X-wind paradigm the disc is devoid of any large-scale magnetic field, reducing the launching radii to its innermost annuli, the extended disc wind is characterized by a magnetic field which threads the disc on a large radial extension. Given that both the range of the ejection region and the shape of the Alfvén surface are different [compare for example fig. 11 in Tzeferacos et al. (2009) and fig. 1 in Shang et al. (1998)], the predicted terminal velocities, ejection efficiencies and angular momentum fluxes will also diverge.

Compared to our disc winds, published outflow solutions from the X-region obtain a smaller range of magnetic lever arms and their typical values are lower [$\lambda \simeq 3-6$, fig. 1 in Shang et al. (1998); similar values can be inferred from figs 12(c) and 15(c) in Romanova et al. (2009)]. Moreover, since the launch only occurs at small radii near the co-rotation point, the available Keplerian angular momentum is relatively small. This results in winds that carry 10−100 times less specific angular momentum compared to our extended winds (see also fig. 3 in Ferreira et al. 2006). In the outflow's launching region the viscous torque is at most comparable to that of the jet (Romanova et al. 2009), whereas in the angular momentum budget of our simulations the wind's torque is always dominant (Table 4). This discrepancy can also be attributed to the magnetic Prantl number used in Romanova et al. (2009), which is relatively elevated with respect to ours.

Conversely, the ejection efficiency values found for both X-winds and conical winds are systematically larger than those seen in Table 3. For example, in Shu et al. (1994) they derive $\dot{M}_{\rm ej}/\dot{M}_{\rm acc} \simeq 0.33$ whereas in Romanova et al. (2009) and Lii et al. (2012) they report $\dot{M}_{\rm ej}/\dot{M}_{\rm acc} \simeq 0.2$. It should be noted though that these values constitute *upper limits*, since viscous effects in the disc remain uncertain (Ostriker & Shu 1995).

The terminal speeds predicted by both types of models can be conveniently recovered using $V_{p,\infty} \approx V_0\sqrt{2\lambda - 3}$ (equivalent also to equation 4.12 in Shu et al. 1994), where $V_0 = \Omega_0 r_0$ is the rotation velocity of the magnetic field's footpoint r_0. In the case of X-winds, we have $\Omega_0 r_0 \simeq \Omega_x r_x$ (namely the rotation velocity at the co-rotation point) and a relatively small span of lever arms, which results in a specific range of velocities. In our simulations, however, we obtain a broader spectrum of poloidal speeds due to the range of Keplerian velocities ($V_0 \approx V_{\rm K0}$) in the extended launching region.

Comparison with YSO data. It has been known since the studies of Garcia et al. (2001) and Pesenti et al. (2004) that 'cold' disc winds, with magnetic lever arms larger than 50, cannot effectively model YSO jet observations, since they predict too large rotation rates and terminal velocities. Recent investigations in the literature, such as the observations of DG Tau (Bacciotti et al. 2002), RW Aur (Coffey et al. 2004; Woitas et al. 2005; Ferreira et al. 2006) and TH 28 (Coffey et al. 2004), can provide stringent constrains for our simulations. In those jets, the velocities observed vary greatly, ranging from $<$100 up to $\geq$500 km s^{-1}. According to the asymptotic relation $V_{p,\infty} \approx V_{\rm K0}\sqrt{2\lambda - 3}$, the disc-wind terminal speed is controlled by: (i) the λ parameter, which is in turn determined by the mass ejection-to-accretion ratio as it has been shown in this paper, and (ii) the toroidal velocity of the (Keplerian) disc $V_{\rm K0}$ in the launching region. Outflows launched from relatively larger disc radii tend to be characterized by a smaller terminal speed but, correspondingly, a larger specific angular momentum.

For instance, the object TH 28-Blue (blueshifted lobe; Coffey et al. 2004; Ferreira et al. 2006, originating from a central star of $M \sim 1\,{\rm M}_\odot$) shows velocities in the range 270–500 km s^{-1} and $\lambda \geq 4-16$. In the simulations presented, solutions with small amount of turbulent heating ($\bar{f}$ close to unity) can account for the faster branch of jets: assuming a central attractor of $M \sim 1\,{\rm M}_\odot$ and an ejection region of 1 au the obtained velocities are $\sim$290 and 260 km s^{-1}. Also the numerically obtained values of the magnetic lever arms are $\sim$14–16 (also see Table 3). Conversely, the object DG Tau-Blue with $M \sim 0.67\,{\rm M}_\odot$ (Bacciotti et al. 2002) is much slower, its moderate velocity peaking at $\sim$70 km s^{-1} and with $\lambda \geq$ 4–8, which agrees with our warmer cases of $\bar{f} \sim 0.4$ with $\lambda \sim 4$ and an ejection region of 1 au. On the other hand, the observationally inferred specific angular momentum seems to suggest that this outflow could be also characterized by a larger lever arm and a larger launching radius ($\sim$2 au; Ferreira et al. 2006), as previously discussed. Only precise observational constraints on the outflow specific angular momentum and the mass ejection/accretion efficiency could help to distinguish between these possibilities. Whichever the case though, this study confirms that T Tauri jets are connected with *extended* 'warm' disc winds, stemming from regions between 0.1 au and several au from the central object (Ferreira et al. 2006; Stute et al. 2008). Moreover, the ejection rates obtained from the simulations are in good agreement with the upper limits that can be derived from the λ lower limits (see equation 17 in Ferreira et al. 2006).

It should be noted at this point that a disparity in the ejection efficiency, induced by the mass load variation due to disc heating, could be an alternative explanation of the speed discrepancy seen in the blue- and redshifted lobes of objects such as TH 28 or RW Aur (see Ferreira et al. 2006 for other mechanisms). This however can only apply to objects that exhibit an even larger discrepancy in the ejection rate between lobes. In order to study such an option, the equatorial symmetry should be lifted and allow for some anisotropy between the two disc halves. Such investigations have already been performed by Lovelace et al. (2010) and Matsakos et al. (2012), while exploring the effects of complex magnetic field topologies at the star region.

Comparison with AGN data. The impossibility of high-resolution observations for AGN jets, at most down to parsec scales, makes comparison with these observations somewhat more uncertain, since our simulations refer to milli-parsec scales. Assuming a fiducial mass for the central black hole of $\sim 10^8\,{\rm M}_\odot$, the values obtained for the usual relativistic parameters $\beta = u/c$ and $\gamma = 1/\sqrt{1-\beta^2}$ are in the range $0.39 \leq \beta \leq 0.72$ and $1.09 \leq \gamma \leq 1.44$, respectively, for $0.4 \leq \bar{f} \leq 1$. These values are obviously small for AGN jets at parsec scales; however, for the radio galaxy NGC 6251, Sudou et al. (2000) inferred a bulk acceleration from $\beta = 0.13$ to 0.42 on sub-parsec scales, compatible with our intermediate 'warm' solutions. Since the magnetic energy is not fully converted into kinetic (upper panel of Fig. 6), there is still room for acceleration and larger bulk velocities farther away (see also Vlahakis & Königl 2004). In any case, even converting all the available magnetic energy the terminal jet velocity could reach only mildly relativistic values. For example, since $(\lambda - 3/2)V_{\rm K0}^2 \sim (\gamma_\infty - 1)c^2$, our coldest cases ($\bar{f} = 0.8, 1$) with $\lambda \sim 11-15$ would exhibit an asymptotic $\gamma_\infty \sim 1.47-1.67$ which is only compatible with rather slow Fanaroff–Riley type I sources such as 3C 338 ($\beta \sim 0.8, \gamma \sim 1.7$) at parsec scales (Giovannini et al. 2001).

These solutions cannot account for ultrarelativistic sources like the quasars 3C 279 (Piner et al. 2003 with $\gamma \sim 13$), 3C 345 (Unwin et al. 1997 with $\gamma \sim 10$) or even more powerful blazars such as 1510-089 (Jorstad et al. 2005 with $\gamma \sim 36$). Such jets most likely require a relativistic modelling of the innermost orbits to be properly addressed (see for example Camenzind 1986; Vlahakis & Königl 2004 or Fendt & Ouyed 2004; Komissarov et al. 2007, 2009;

Downloaded from http://mnras.oxfordjournals.org/ at Uni Torino Dip Sanità Pubblica Microbiologia on February 19, 2013

Keppens et al. 2008; Mignone et al. 2010; Porth & Fendt 2010 for analytical and numerical approaches). Even if the ultrarelativistic jet component can only originate from the innermost regions and/or the black hole, the extended disc wind found by our simulations contributes to the system's energy budget.

ACKNOWLEDGMENTS

PT would like to thank Prof. Max Camenzind for his hospitality during the stay in Landessternwarte Königstuhl (LSW) of Heidelberg, Germany, while working on this project. The authors would like to thank the reviewer for valuable comments. This study was funded by the interuniversity consortium CINECA, Bologna, Italy. The authors acknowledge financial contribution from the agreement ASI-INAF I/009/10/0. All simulations have been performed at the High Performance Computing Center Stuttgart (HLRS), Germany, under the HPC Europa 2 project (project number 228398) with the support of the European Commission – Capacities Area – Research Infrastructure.

REFERENCES

Bacciotti F., Ray T. P., Mundt R., Eislöffel J., Solf J., 2002, ApJ, 576, 222
Balbus A. S., Hawley J. F., 1991, ApJ, 376, 214
Blandford R. D., 1976, MNRAS, 176, 465
Blandford R., Begelman M., 1999, MNRAS, 303, 1
Blandford R. D., Payne D. G., 1982, MNRAS, 199, 883
Camenzind M., 1986, A&A, 156, 137
Casse F., Ferreira J., 2000a, A&A, 353, 1115
Casse F., Ferreira J., 2000b, A&A, 361, 1178
Casse F., Keppens R., 2002, ApJ, 581, 988
Casse F., Keppens R., 2004, ApJ, 601, 90
Coffey D., Bacciotti F., Woitas J., Ray T. P., Eislöffel J., 2004, ApJ, 604, 758
Combet C., Ferreira J., 2008, A&A, 479, 481
Contopoulos J., Lovelace R. V. E., 1994, ApJ, 429, 139
Di Matteo T., Quataert E., Allen S. W., Narayan R., Fabian A. C., 2000, MNRAS, 311, 507
Di Matteo T., Allen S. W., Fabian A. C., Wilson A. S., Young A. J., 2003, ApJ, 582, 133
Donnaruma I. et al., 2009, ApJ, 707, 1115
Fendt C., Ouyed R., 2004, ApJ, 608, 378
Ferreira J., 1997, A&A, 319, 340
Ferreira J., 2002, EAS Publications Series, 3, 229
Ferreira J., Casse F., 2004, ApJ, 601, L139
Ferreira J., Pelletier G., 1995, A&A, 295, 807
Ferreira J., Dougados C., Cabrit S., 2006, A&A, 453, 785
Garcia P. J. V., Cabrit S., Ferreira J., Binette L., 2001, A&A, 377, 609
Giovannini G., Cotton W. D., Feretti L., Lara L., Venturi T., 2001, ApJ, 552, 508
Goedbloed J. P., Beliën A. J. C., van der Holst B., Keppens R., 2004, Phys. Plasmas, 11, 28
Jorstad S. G. et al., 2005, ApJ, 130, 1418
Kato S. X., Kudoh T., Shibata K., 2002, ApJ, 565, 1035
Keppens R., Casse F., Goedbloed J. P., 2002, ApJ, 569, L121
Keppens R., Meliani Z., van der Holst B., Casse F., 2008, A&A, 486, 663
Komissarov S., Barkov M. V., Vlahakis N., Königl A., 2007, MNRAS, 380, 51
Komissarov S., Vlahakis N., Königl A., Barkov M. V., 2009, MNRAS, 394, 1182
Königl A., Romanova M. M., Lovelace R. V. E., 2011, MNRAS, 416, 757
Lesur G., Longaretti P., 2009, A&A, 504, 309
Lii P., Romanova M., Lovelace R., 2012, MNRAS, 420, 2020
Li Z.-Y., 1995, ApJ, 444, 848
Londrillo P., Del Zanna L., 2004, J. Comput. Phys., 195, 17
Lovelace R. V. E., 1976, Nat, 262, 649
Lovelace R. V. E., Berk H. L., Contopoulos J., 1991, ApJ, 379, 696
Lovelace R. V. E., Romanova M. M., Ustyugova G. V., Koldoba A. V., 2010, MNRAS, 408, 2083
Matsakos T., Tsinganos K., Vlahakis N., Massaglia S., Mignone A., Trussoni E., 2008, A&A, 477, 521
Matsakos T., Massaglia S., Trussoni E., Tsinganos K., Vlahakis N., Sauty C., Mignone A., 2009, A&A, 502, 217
Matsakos T. et al., 2012, A&A, 545, 53
Meliani Z., Casse F., Sauty C., 2006, A&A, 460, 1
Mestel L., 1961, MNRAS, 122, 472
Michel F. C., 1969, ApJ, 158, 727
Mignone A., Bodo G., Massaglia S., Matsakos T., Tesileanu O., Zanni C., Ferrari A., 2007, ApJS, 170, 228
Mignone A., Rossi P., Bodo G., Ferrari A., Massaglia S., 2010, MNRAS, 402, 7
Mignone A., Tzeferacos P., Bodo G., 2010, J. Comput. Phys., 229, 5896
Mirabel I. F., Dhawan V., Chaty S., Rodriguez L. F., Marti J., Robinson C. R., Swank J., Geballe T., 1998, A&A, 330, 9
Murphy G. C., Ferreira J., Zanni C., 2010, A&A, 512, 82
Narayan R., Yi I., 1995, ApJ, 444, 231
Ostriker E. C., Shu F. H., 1995, ApJ, 447, 813
Ouyed R., Pudritz R. E., 1997, ApJ, 482, 712
Ouyed R., Pudritz R. E., 1999, MNRAS, 309, 233
Ouyed R., Clarke D. A., Pudritz R. E., 2003, ApJ, 582, 292
Pelletier G., Pudritz R. E., 1992, ApJ, 394, 117
Pesenti N., Dougados C., Cabrit S., Ferreira J., Casse F., Garcia P., O'Brien D., 2004, A&A, 416, L9
Petrucci P. O., Ferreira J., Henri G., Malzac J., Foellmi C., 2010, A&A, 522, 38
Piner B. G., Unwin S. C., Wehrle A. E., Zook A. C., Urry C. M., Gilmore D. M., 2003, ApJ, 588, 716
Porth O., Fendt C., 2010, ApJ, 709, 1100
Romanova M. M., Ustyugova G. V., Koldoba A. V., Chechetkin V. M., Lovelace R. V. E., 1997, ApJ, 482, 708
Romanova M. M., Ustyugova G. V., Koldoba A. V., Lovelace R. V. E., 2009, MNRAS, 399, 1802
Shakura N. I., Sunyaev R. A., 1973, A&A, 24, 337
Shang H., Shu F. H., Glassgold A. E., 1998, ApJ, 493, L91
Shang H., Glassgold A. E., Shu F. H., Lizano S., 2002, ApJ, 564, 853
Shibata K., Uchida Y., 1985, PASJ, 37, 31
Shu F., Najita L., Ostriker E., Wilkin F., Ruden S., Lizano S., 1994, ApJ, 429, 781
Stone J. M., Norman M. L., 1994, ApJ, 433, 746
Stute M., Tsinganos K., Vlahakis N., Matsakos T., Gracia J., 2008, A&A, 491, 339
Sudou H., Taniguchi Y., Ohyama Y., Kameno S., Sawada-Satoh S., Inoue M., Kaburaki O., Sasao T., 2000, PASJ, 52, 989
Tsinganos K., 1982, ApJ, 252, 775
Tsinganos K., Trussoni E., 1990, A&A, 231, 270
Tzeferacos P., Ferrari A., Mignone A., Zanni C., Bodo G., Massaglia S., 2009, MNRAS, 400, 820
Uchida Y., Shibata K., 1985, PASJ, 37, 515
Unwin S. C., Wehrle A. E., Lobanov A. P., Zensus J. A., Madejski G. M., Aller M. F., Aller H. D., 1997, ApJ, 480, 596
Ustyugova G. V., Koldoba A. V., Romanova M. M., Chechetkin V. M., Lovelace R. V. E., 1999, ApJ, 516, 221
Vercellone S. et al., 2011, ApJ, 736, 38
Vlahakis N., Königl A., 2004, ApJ, 605, 656
Vlahakis N., Tsinganos K., 1998, MNRAS, 298, 777
Vlahakis N., Tsinganos K., Sauty C., Trussoni E., 2000, MNRAS, 318, 417
Weber E. J., Davis L., 1967, ApJ, 148, 217
Woitas J., Bacciotti F., Ray T. P., Marconi A., Coffey D., Eislöffel J., 2005, A&A, 432, 149
Zanni C., Ferrari A., Rosner R., Bodo G., Massaglia S., 2007, A&A, 469, 811

This paper has been typeset from a TEX/LATEX file prepared by the author.

Downloaded from http://mnras.oxfordjournals.org/ at Uni Torino Dip Sanità Pubblica Microbiologia on February 19, 2013